Rapid Thermal Annealing of p-Type Polysilicon Passivated Contacts Silicon Solar Cells

Arpan Sinha, *Graduate Student Member, IEEE*, Sagnik Dasgupta, *Graduate Student Member, IEEE*, Ajeet Rohatgi, *Life Fellow, IEEE*, and Mool C. Gupta, *Fellow, IEEE*

***Abstract*—The carrier selective contacts Si solar cells based on tunnel oxide passivated contact (TOPCon) have provided an efficiency of over 25%, and the large-scale production is planned. One of the crucial steps in TOPCon solar cells fabrication is furnace annealing at around 875 °C. We have investigated the rapid thermal annealing (RTA) for TOPCon solar cells. We discovered that the RTA carried out in air showed much fewer hydrogen-induced blisters than in the N_2 atmosphere. Second, the optical radiation and heat generated in RTA had a significant effect on the degradation of iV_{oc}. The RTA with a SiN_x:H layer on top of polysilicon generated iV_{oc} of 706 mV. The mechanism of degradation under air versus nitrogen atmosphere and the effect of high-intensity light during the annealing process were inferred through various characterizations, such as surface morphology, surface passivation, crystallinity determination, chemical compositional changes, electrical sheet resistances, and oxidation state of ultrathin SiO_x. The TOPCon after air RTA performed better than in nitrogen, optimally at 825 °C. Forming gas annealing further improved the iV_{oc}. Crystallization and sheet resistance were dependent on the annealing temperature and time.**

***Index Terms*—Annealing, blister, polysilicon, rapid thermal annealing (RTA), solar cells, tunnel oxide passivated contact (TOPCon).**

I. Introduction

THE architecture of high-efficiency c-Si-solar cells based on tunnel oxide passivated contact (TOPCon) generally consists of stack layers of heavily doped (B-doped or P-doped) polycrystalline silicon (poly-Si) layer and ultrathin oxide SiO_2 on the doped c-Si substrate. Although the term TOPCon was coined under the assumption of tunneling current as the charge transport mechanism in these selective contacts, several publications show that the dominating current transport mechanism is through the pinholes formed during the annealing process [1], [2]. There are many parameters and constraints in the fabrication steps that influence the intrinsic open-circuit voltage (iV_{oc}) and efficiency of a solar cell.

The recent research laboratory record-breaking efficiencies of p-TOPCon (based on p-type Si wafer) and n-TOPCon (based on n-type Si wafer) solar cells are 26.1% and 25.8%, respectively [3], [4]. The thermal annealing is a very important fabrication step required for achieving polycrystallization dopant activation and minimizing interfacial defects by improved passivation, thus enhancing the iV_{oc} and efficiency of a TOPCon solar cell.

Previously, the traditional tube-furnace annealing was used for thermal annealing of n- and p-TOPCon at high temperatures under inert atmospheres, such as N_2 [5], [6], [7], [8], [9], [10] [11]. The thermal processing with heating durations of tens of minutes is widely used in photovoltaic device fabrication and even in some of the industrial processes for $POCl_3$ diffusion. The firing process of the metallization, which includes heating, dwell, and cooling, is done in tens of seconds. Borden et al. [12] reported a firing process of 30 s for their poly-Si contacts. The blister formation is an important bottleneck in the fabrication of TOPCon architectures as under intense dehydrogenation pressure, the physical rupturing of ultrathin SiO_x and poly-Si layers occurs. This results in the degradations of the passivation quality [6]. Ingenito et al. [13] described even faster processes while addressing the minimization of the blistering formation issue. Recent reports have shown that the rapid thermal annealing (RTA) has been used for annealing purposes in n- and p-TOPCon fabrication [14], [15], [16]. Rapid annealing is focused on time duration from a few seconds to several minutes. RTA has a fundamental advantage of a short period of annealing time as compared with tube-furnace annealing. Yang et al. [15] reported blister formations during RTA of n-TOPCon solar cells. Although earlier studies have been on suppressing blisters, there is a lack of a comprehensive study on blister formation under the RTA and the role of different atmospheres, such as air versus nitrogen, for p-TOPCon structures [13], [17].

In the RTA chamber, the a-Si:H layer in the TOPCon device faces direct exposure to the intense lamp light and heat for the whole period of rapid annealing. In such circumstances, the effect of intense light intensity under heat during RTA needs to be investigated.

Different dielectric capping layers of SiN_x:H and Al_2O_3 and thermal annealing steps have been known to be excellent hydrogenation sources for passivating TOPCon structures using tube furnaces [18], [19], [20], [21], [22]. Moreover, dielectric layers protect TOPCon structures from spiking and damage during

Manuscript received 21 November 2022; accepted 30 January 2023. Date of publication 14 February 2023; date of current version 20 April 2023. This work was supported by the National Science Foundation (NSF) under Grant ECCS-2005098 and Grant I/UCRC-1338917. *(Corresponding author: Mool C. Gupta.)*

Arpan Sinha and Mool C. Gupta are with the Department of Electrical and Computer Engineering, University of Virginia, Charlottesville, VA 22904 USA (e-mail: as2ag@virginia.edu; mgupta@virginia.edu).

Sagnik Dasgupta and Ajeet Rohatgi are with the School of Electrical and Computer Engineering, Georgia Institute of Technology, Atlanta, GA 30332 USA (e-mail: sdasgupta@gatech.edu; ajeet.rohatgi@ece.gatech.edu).

Color versions of one or more figures in this article are available at https://doi.org/10.1109/JPHOTOV.2023.3241790.

Digital Object Identifier 10.1109/JPHOTOV.2023.3241790

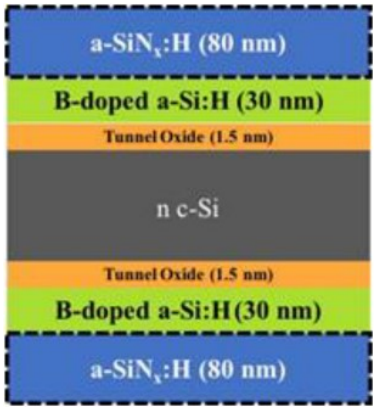

Fig. 1. Schematic diagram of a fabricated TOPCon test structure. The dotted a-SiN_x:H layers are considered when the test structure is TOPCon/SiN_x:H.

screen-printing metallization [23]. Therefore, it is necessary to investigate the utility of using the dielectric SiN_x:H layer.

In this article, we present the results of RTA under air versus N_2 and the effect of high-intensity light under heat on *in situ* B-doped p-TOPCon solar cells. The mechanism of passivation degradation was investigated through various measurements, such as surface morphology, carrier lifetime, crystallinity, chemical compositional changes, electrical sheet resistances, and oxidation state of SiO_x.

II. Experiment

A. Fabrication of the p-TOPCon Test Structure

The p-TOPCon architecture used here is based on the type of poly-Si layer (*in situ* B-doped poly-Si/SiO_x stack) on n-type c-Si wafers. The *in situ* boron doping has several advantages over *ex situ* boron doping, such as simplicity, independent of dopant predeposition process, higher throughput, higher deposition rate of poly-Si layer, higher boron concentration, higher field-induced passivation, and lower optimal annealing temperature [24], [25], [26]. Fig. 1 shows the schematic diagram of the TOPCon test structure and with SiN_x:H layer (dotted). These test structures were fabricated on 200 μm thick n-type monocrystalline Cz-type <100> silicon wafers with a bulk resistivity of 3.2 Ω·cm. Saw damage was removed in 9% wt. KOH at 80 °C for 12 min resulting in a semiplanarized surface. Wafers were cleaned in piranha solution (96% wt. H_2SO_4: H_2O_2: DI :: 1:1:2) and SC-2 (38% wt. HCl: H_2O_2: DI :: 1:1:2) along with oxide removal (5% wt. HF solution) between each step and at the end. The solution temperature was between 50 and 60 °C. Subsequently, an ultrathin (~1.5 nm) layer of SiO_x was grown on both sides of Si in 70% wt. electronics grade HNO_3 at 100 °C for 15 min. *In situ* boron-doped polysilicon was then grown on both sides of the wafer in a Tystar tube low pressure chemical vapor deposition (LPCVD) system at 530 °C for 27 min using precursor gases of silane and diborane resulting in a thickness of approximately 30 nm. A selected sample was annealed in nitrogen at 875 °C for 30 min in a Centrotherm tube furnace to improve crystallinity and activate dopants. Additionally, some samples were coated with 80 nm of SiN_x:H layer on both sides in a Centrotherm plasma enhanced chemical vapor deposition (PECVD) reactor for improved passivation due to hydrogenation.

The samples were cut into a 1 cm × 1 cm area from a single 6-in test wafer before the start of any further processing. The quasi-steady-state photoconductance (QSSPC) measurements were done on 1 in^2 test samples. The QSSPC sensor coil diameter was 4 cm. Three samples were prepared for each thermal annealing test. The maximum film thickness variation over 1 cm length was found to be ±5%. The boron concentration homogeneity was not measured.

Both the RTAs and forming gas anneals (FGAs) were done in the AnnealSys rapid thermal processing (RTP) system under different processing gas environments, such as ultrapure N_2 and forming gas (5% H_2: 95% Ar) from Praxair. In the case of air annealing, the surrounding air was used with no pumping. The humidity recorded in the room was 40%–42%. The temperature regime for breaking Si-H bonds and dehydrogenation is from 300 to 550 °C, and a slower heating rate is beneficial to avoid blister formations [27]. All the RTAs were done using the three-step process, where the first step of annealing started with a 30-min ramp-up from room temperature to 350 °C and dwelling for further 30 min, followed by the second step of a 30-min ramp-up to 500 °C and dwell there for further 30 min. Subsequently, the final step was a 10-min ramp-up to different annealing temperatures, such as 625, 750, 825, and 875 °C, for a 5-min dwell time. The RTAs were done both in N_2 and air atmospheres. The three-step method was adapted from Lee et al.'s article [17], but their study was limited only to the tube-furnace annealing. The reference samples were annealed in the tube furnace at 875 °C for 30 min in N_2 with a ramp-up from 600 °C at the rate of ~10 °C/min. The cooling rate in the RTA was ~300 °C/min as compared with ~3 °C/min in the tube furnace. This fast cooling rate emphasizes the rapidity of our RTA processing. The FGA process consisted of annealing treatment at 425 °C in forming gas for 1 h. To investigate the light-induced damaging effects due to the direct exposure from the tungsten-halogen lamp in the RTA system, a 500 μm thick p-type c-Si wafer cover of 1.05″ × 1.05″ area was placed over the test samples during all the annealing, irrespective of the anneal atmospheres. It was ensured that there was no actual physical contact between the Si wafer cover and the test sample by using small Si spacers. Test samples were annealed with direct exposure to the light using the three-step process of RTA at 875 °C both in N_2 and air in order to investigate the effect of light-induced degradation. The sample with SiN_x:H layer was directly annealed in RTA at 825 °C in N_2, followed by FGA.

B. Characterizations

Except for the QSSPC iV_{oc} measurements, all the characterization studies were accomplished using 1 cm^2 area test samples. The SEM surface morphology was characterized using a 15° stage tilt in FEI Quanta 650 Field Emission Scanning Electron Microscope. The QSSPC iV_{oc} measurements were conducted on (1″ × 1″) area test samples using WCT-120 Silicon Wafer Lifetime Tester made by Sinton Instruments. The iV_{oc} data were generated at 1 Sun condition. The photoluminescence (PL) setup for passivation characterization consisted of a 532 nm wavelength and 2 W continuous-wave laser (Melles Griot) as an excitation source with a spot size of ~1 mm, a spectrometer Horiba Jobin Yvon iHR320 operated by SynerJY v3.5

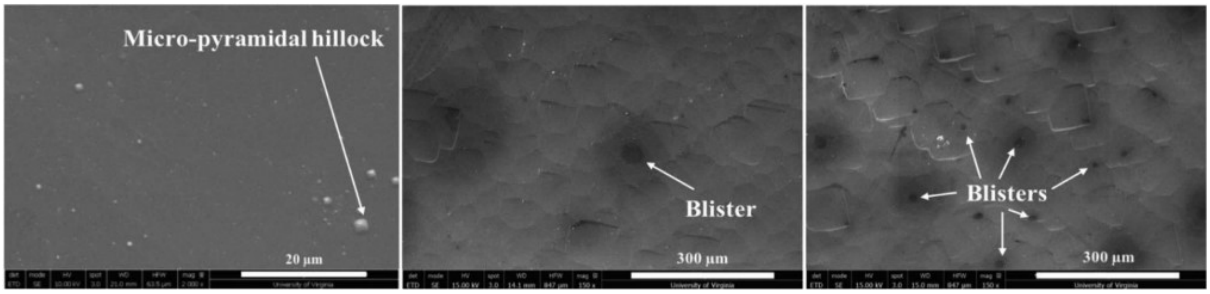

Fig. 2. Top-view SEM images of (a) as-deposited sample, (b) blisters (black areas) after RTA at 875 °C in air, and (c) blisters (black areas) after RTA at 875 °C in N_2.

software, an InGaAs detector, and an SR830 DSP lock-in amplifier (Stanford Research Systems). The excitation laser power was reduced to 70 mW by neutral density filters and quartz glass reflection so that it does not saturate the PL detector, does not heat the test samples significantly, and provides a high S/N ratio. Each PL spectrum reading consisted of an average of ten scans. The absolute PL intensity values are arbitrary but can be used for a relative comparison of the passivation quality. The PL intensity has a peak value at ∼1150 nm due to the c-Si bandgap of ∼1.1 eV [28]. The μ-PL measurement (with a spot size of ∼150 μm) was also done to characterize and differentiate the passivation quality on the blisters and outside-the-blister region. The PL data had an approximate intensity error of ∼2.6%. The Raman spectroscopy for crystallinity measurements was done on Renishaw InVia TM Confocal Raman Microscope with a 405 nm excitation wavelength laser and spot size of 1.8 μm. All Raman scattering data had been taken as an average of ten scans with each of 15 s of acquisition time. To calculate the Raman peak "area under the curve," a reference sample was used every time before making measurements on test samples to account for the changes due to optics, mounting effects, crystallinity, etc. The sheet resistances were measured by Jandel four-point probe station for electrical characterization. The Fourier transform infrared (FTIR) spectroscopy was done in Thermo Scientific Nicolet iS50 FT-IR for chemical compositional characterization. Each FTIR reading was taken as an average of 256 scans, and the background readings were taken as an average of 200 scans. All these characterizations had an error of ∼5%. The X-ray photoelectron spectroscopy (XPS) characterization was done for quantitative surface chemical and elemental composition, depth profiling, and oxidation state determination on PHI Versaprobe III scanning X-ray photoelectron spectrometer with a spot size of ∼200 μm and Al monochromatic X-ray source. The pass energy was 280 eV with a 0.5 eV acquisition step. All the XPS spectra for TOPCon structures had C (1s) peak calibrated to 284.8 eV according to ASTM/NIST [29]. The XPS spectra for the TOPCon/SiN_x:H samples had N(1s) peak calibrated to 397.86 eV [30]. The error bar of XPS measurements for oxidation states of SiO_x was approximately 0.2 eV.

III. Results and Discussion

We present the results of the RTA of p-TOPCon with and without SiN_x:H layer under N_2 versus air and the effects of high-intensity light environment.

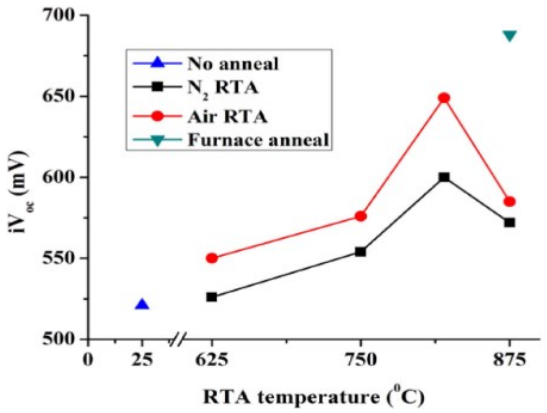

Fig. 3. Graph showing the dependence of iV_{oc} on the RTA temperatures. The data are given for RTA both in N_2 and air atmospheres. The graphs also show the iV_{oc} value for the sample with no annealing and after furnace annealing.

A. Study of the Effects of RTA Atmospheres

1) Surface Morphology: Fig. 2(a) shows the top-view image of as-deposited samples. No blisters were observed except for the octahedral pyramidal features on the surface. The pyramidal structures were caused due to the KOH etching during the semiplanarization process, and they were unaffected by annealing temperatures and time conditions. Schröder et al. [31] have reported the observation and possible mechanism of such pyramidal features during the KOH etching of Si. Fig. 2(b) shows the top-view SEM image of blisters on the air-annealed samples at 875 °C. A higher number density of such similar blisters was observed in the N_2-annealed test samples at 875 °C, as shown in Fig. 2(c). The blisters covered ∼1% of the total surface area of air-annealed samples, whereas the blisters covered ∼3%–4% of the total surface area of N_2-annealed samples. The morphology of samples annealed in the tube furnace is not shown here as no change was noted.

The high-temperature annealing caused the dissociation of Si-H bonds, which resulted in the release of atomic hydrogen in the poly-Si/SiO_x/c-Si stack. These atomic hydrogens combined to form molecular H_2 under its own immense pressure and consequently escaped while rupturing through the polysilicon layer in the form of blisters [32]. The three-step process of lower temperature annealing minimized the formation of blisters. The furnace-annealed samples showed fewer blisters possibly due to slower heating rates compared with the RTA.

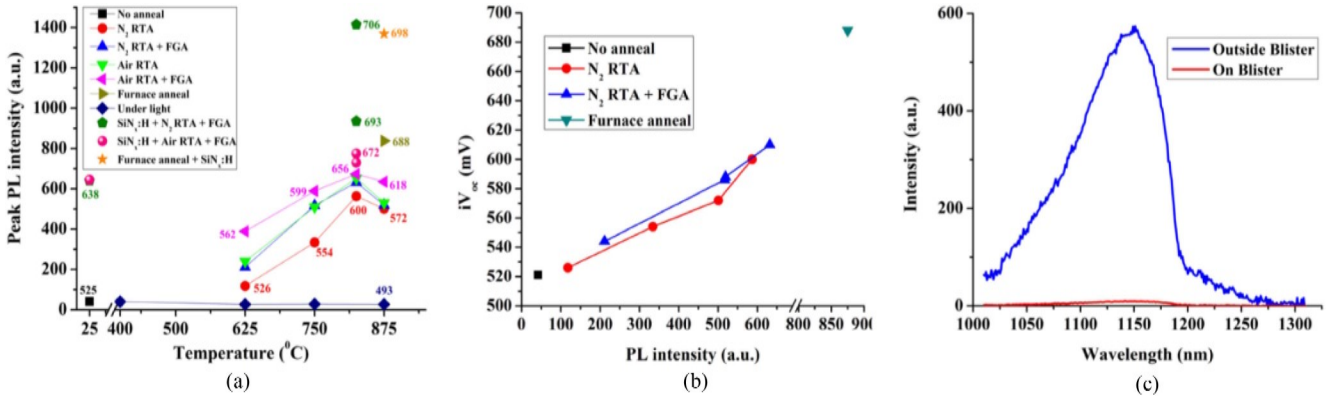

Fig. 4. (a) Qualitative dependence of peak PL intensity on the RTA temperatures for various annealing conditions. The iV_{oc} (in mV) numbers are provided on the graph and (b) dependence of iV_{oc} on the peak PL intensity. The data are given for RTA in N_2 and subsequent FGA only, and (c) PL intensity on and outside blister areas.

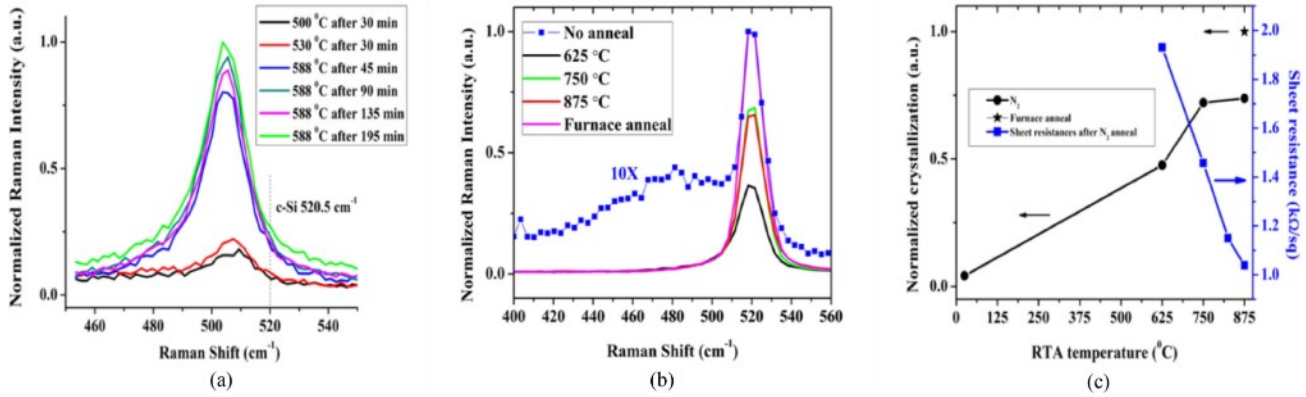

Fig. 5. (a) Raman spectra for the dependence of crystallization of a-Si:H on the anneal time duration while the sample was kept at hot stage at various temperatures. (b) Room temperature Raman spectra for the dependence of crystallization on the RTA temperature, anneal time was 5 min and curves are normalized to furnace anneal. The as-deposited sample curve is magnified ten times due to lower Raman intensity and (c) growth of crystallinity (area under curve) as a function of temperature.

2) Surface Passivation Quality: Fig. 3 shows the variation of iV_{oc} with the RTA temperatures under N_2 and air. The optimal regime of annealing temperature was found to be near 825 °C, and the iV_{oc} started decreasing at temperatures beyond 825 °C. This could be due to the possible degradation to the SiO_2 passivation layer. The iV_{oc} peak value was higher in the air (649 mV) than in N_2 (600 mV). Since the *in situ* B-doped poly-Si layers of these test samples were fabricated by the LPCVD process at a lower temperature of 530 °C, there was a significant starting amount of hydrogen, which increased the chances of blister formations. The RTA sample did not reach the tube-furnace-annealed sample iV_{oc} value of 688 mV, possibly due to the higher density of blisters leading to the passivation degradation.

3) Photoluminescence: Fig. 4(a) shows the variation of peak PL intensity w.r.t. RTA temperatures in the N_2 and air atmosphere and FGAs. It was observed that the annealing temperature of 825 °C provided the highest PL intensity, and FGA improved it further. In N_2-annealed test sample, the highest PL intensity was 563 a.u. and FGA pushed it to 632 a.u. Similarly, in the case of air anneal, the highest PL intensity was 652 a.u. and FGA helped to reach 673 a.u. The furnace-annealed sample had a higher peak PL intensity. This showed that the passivation quality of air-annealed samples was better than that of N_2. Fig. 4(b) shows the observed relationship between iV_{oc} and peak PL intensity. Note when the junction is present, a logarithmic relationship is expected [33]. However, in this case, the PL change occurs due to the oxidation, crystallinity increase, and decrease in defect density. Therefore, it shows a linear relationship.

Fig. 4(c) shows the μ-PL intensity between the blister region and outside the blister region. It was found that the peak PL intensity at the blister region was 9 a.u. as compared with ~570 a.u. outside the blister region of an air-annealed test sample at 825 °C. This showed that the blisters caused extensive passivation degradation in the test samples.

4) Crystallinity Determination: Fig. 5(a) shows the Raman peak intensity of the polycrystalline phase w.r.t. anneal temperature and time duration in the N_2 atmosphere. Choi et al. [6] reported that the deposition temperature of LPCVD poly-Si should be above 580 °C to ensure lower hydrogen content that prevents blister formation. An increase in crystallinity was observed starting at 588 °C, shown by the Raman peak at 508 cm^{-1}, and it increased further as the annealing time was increased. These measurements were carried out in a heated chamber filled

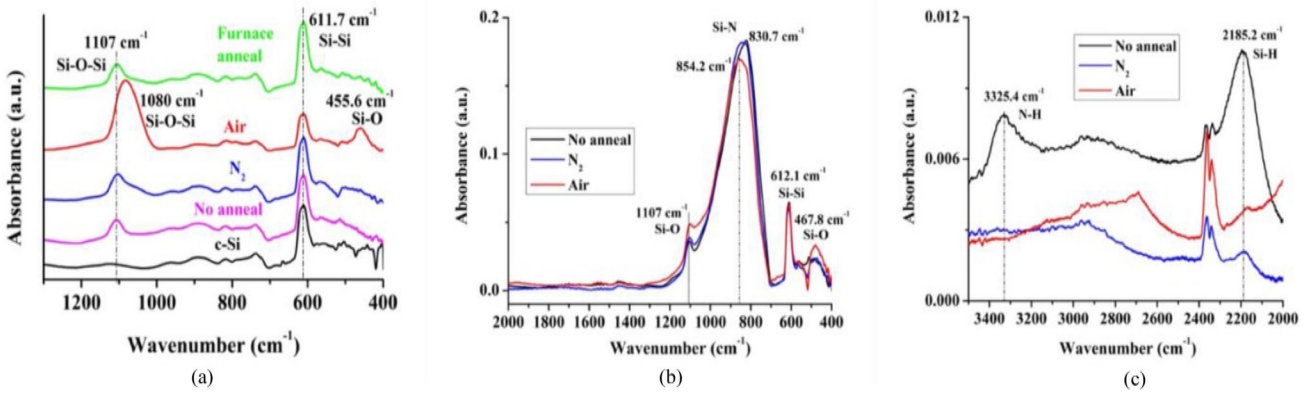

Fig. 6. (a) FTIR spectra for c-Si, TOPCon samples annealed at 825 °C in N_2 and air and results are compared with furnace-annealed sample. (b) FTIR spectra for TOPCon/SiN_x:H samples as deposited and annealed at 825 °C in N_2 and air. (c) FTIR spectra for TOPCon/SiN_x:H samples from 3400 to 2000 cm^{-1} wavenumber region. All the samples were FGA treated before FTIR.

with N_2. The standard room temperature Raman peak of c-Si at 520.5 cm^{-1} is shifted to 508 cm^{-1} due to the measurements done at the high temperature [34]. The as-deposited *in situ* B-doped poly-Si film was a mixture of amorphous and polycrystalline phases. Fig. 5(b) shows the change of a-Si:H peak Raman peak at 480 cm^{-1} toward the crystalline phase at 519.1 cm^{-1} as the RTA temperature increased from 625 to 875 °C in the N_2 atmosphere. Similar phenomena were observed when the test samples were subjected to RTA under an air atmosphere (not shown here). Fig. 5(c) shows the increase of the "area under the curve" of the Raman curve w.r.t. RTA temperatures in the N_2 atmosphere, indicating the increase in crystallinity. The degree of crystallinity in the in situ B-doped TOPCon depends on RTA temperatures and annealing time, not on anneal atmospheres or postanneal FGAs. At room temperature, the Raman peaks for poly-Si and c-Si substrate both occur at 520.5 cm^{-1}. The Raman peak of poly-Si is much broader than that of c-Si due its polycrystalline nature. At the Raman excitation wavelength of 405 nm, the transmission through 30 nm poly-Si is only ∼12% based on the optical *n* and *k* constants, and therefore, the contribution to the Raman peak from the c-Si substrate was very small.

5) Chemical Composition: Fig. 6(a) shows the FTIR absorbance spectra of c-Si, as-deposited film, TOPCon structure annealed at 825 °C in N_2 and air, and furnace annealed in N_2.

In Fig. 6(a), the absorbance peak at 1107 cm^{-1} generally corresponds to the presence of the vibrational stretching mode of Si-O, indicating the presence of interstitial oxygen and native oxide [35], [36]. The shift of this peak toward the 1080 cm^{-1} peak corresponds to the stretching mode of Si-O-Si and indicates the formation of typical thermal SiO_2 on the surface after air annealing [37], [38]. The peak at 455.6 cm^{-1} for the air-annealed sample corresponds to the rocking-mode vibration of Si-O bonds, which also indicates the formation of SiO_2 [39]. The vibrational state of the Si–Si bond was observed at 611.7 cm^{-1} [40].

The different peak positions indicated that the air annealing converted the top part of the poly-Si layer into the SiO_2 layer. Under the N_2 RTA and furnace annealing, there was no significant SiO_2 formation except native oxide growth.

6) Sheet Resistance: The conversion of the a-Si:H layer to poly-Si will enhance lateral transport of carriers, dopant activation, and passivation. Fig. 5(c) shows the sheet resistances measured at different annealing temperatures in N_2 along with a degree of crystallinity. It was possible to achieve sheet resistances as low as furnace anneal test samples [0.9 kΩ/sq, not shown in Fig. 5(c)]. The sheet resistance of the nonannealed sample was > 1 MΩ/sq. The RTA atmospheres, such as the air, had a negligible effect on the sheet resistance of *in situ* B-doped poly-Si, measured at a constant annealing temperature of 875 °C.

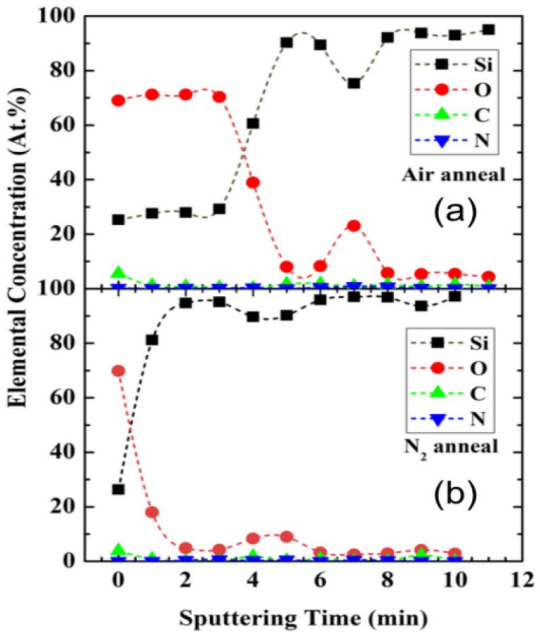

Fig. 7. Depth-profiling XPS spectra showing the atomic percentage profile of (a) air-annealed and (b) N_2-annealed samples based on the atomic concentrations of Si (2p), O (1s), C (1s), and N (1s).

7) Oxidation State and Elemental Composition: The depth-profiling XPS composition spectra of test samples after RTA both in air and N_2 at 825 °C are shown in Fig. 7(a) and (b), respectively. The sputtering rate of SiO_2 is expected to be ∼8.9 nm/min, and the Si/SiO_2 sputter rate ratio was ∼1.1 [41]. Hence, the exact locations of the surface oxide, poly-Si, and buried ultrathin oxide layers are prone to some error due to the

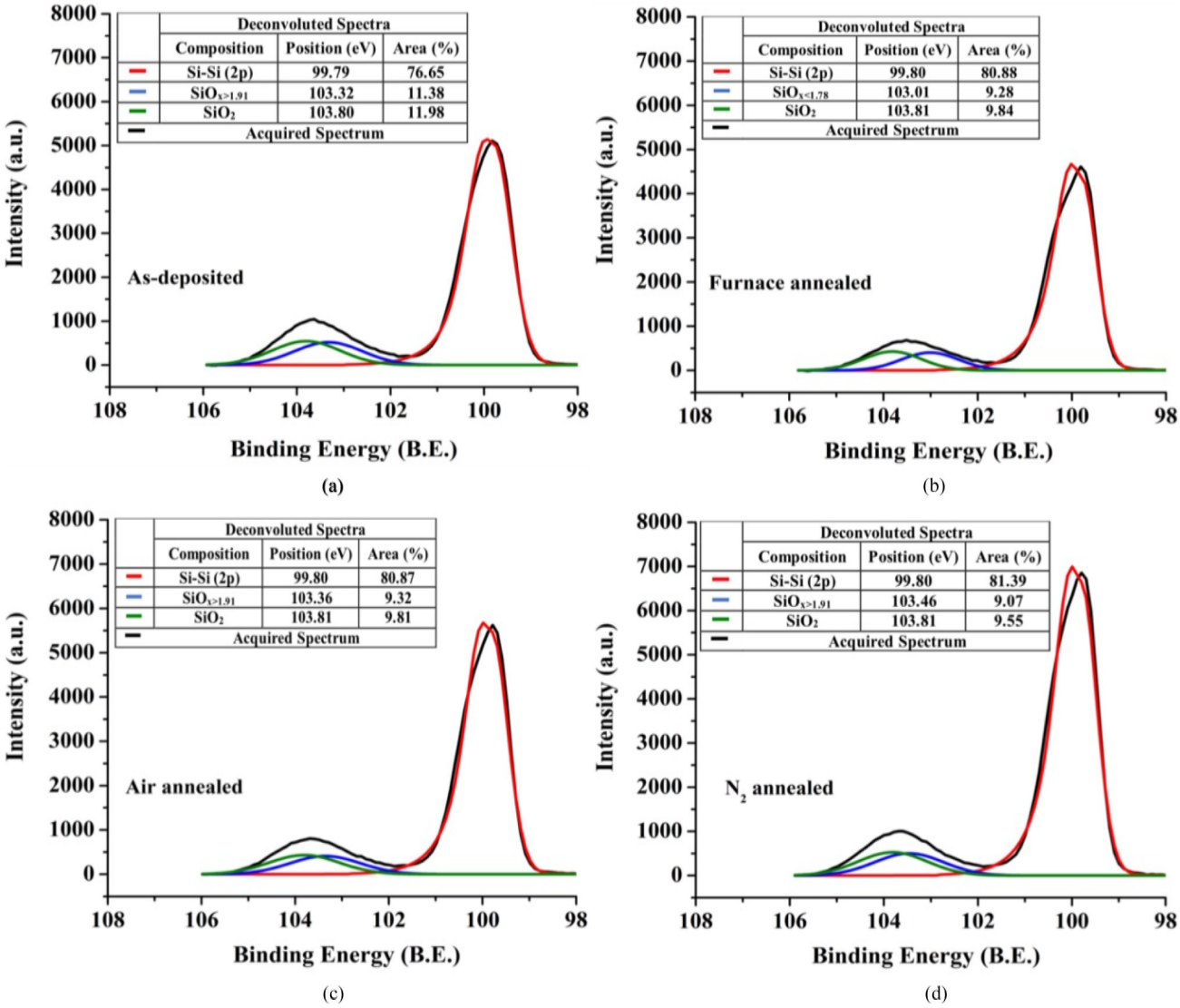

Fig. 8. Surface XPS spectra of ultrathin SiO_2 layer of TOPCon test structures at (a) as-deposited, (b) furnace, (c) air, and (d) N_2 annealing conditions.

undetermined sputter rate through the poly-Si layer. In the case of air annealing, a thicker oxide layer was observed on the top of the remaining poly-Si layer. This proved that the oxygen from air diffused through the surface oxide layer on poly-Si. An increase in oxygen concentration and a decrease in Si concentration under the poly-Si layer is due to the presence of an ultrathin oxide layer. Past the ultrathin oxide/c-Si interface, the Si/O ratio concentration increased. In the case of N_2 annealing, a very thin surface oxide was observed along with the broader peak of Si and oxygen concentrations at the ultrathin oxide region. This shows higher concentration of oxygen present in the ultrathin oxide layer in air-annealed samples. The boron was not able to be detected due to its relatively low concentration. The as-deposited sample had a negligibly thin surface native oxide layer with an intact poly-Si/ ultrathin oxide/c-Si structure (not shown here). This also reiterated our findings from the FTIR study. Fig. 8 shows the XPS spectra of the ultrathin passivating SiO_2 layer after the removal of polysilicon by the chemical etching process for different annealing conditions at 825 °C. XPS spectra show a peak at 99.8 eV due to the Si–Si bond, and another peak at 103.8 eV is due to the presence of the SiO_x layer. The Si-O peak was deconvoluted and showed the two major oxidation states of Si^{3+} and Si^{4+} [42]. The negligible differences in SiO_x/SiO_2 ratios and their respective peak positions suggested that the RTA atmosphere (air or N_2) did not significantly affect the chemical composition of the ultrathin silicon oxide. Only for furnace anneal, there was a visible shift in the Si-O peak. In addition, the area of silicon peak was higher after thermal annealing, indicating the increase in elemental Si [43]. The decrease in SiO_2 concentration was noted, possibly which can come from the incorporation of Si into the oxide layer [44].

B. *Effects of High-Intensity Light Environment*

Initially, the RTA samples showed poor PL intensity and very low iV_{oc} value. It was discovered that the source of poor performance is related to the exposure of samples to the presence of high-intensity light and heat in RTA for sample heating. We

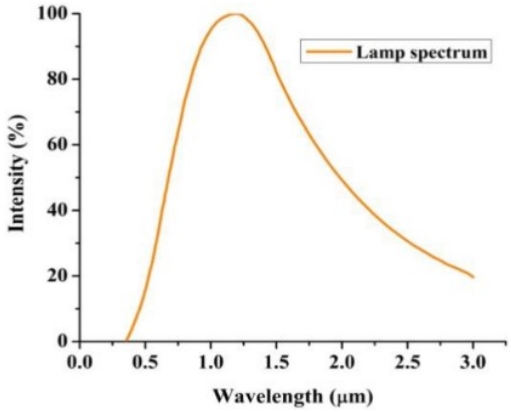

Fig. 9. Spectrum of the RTA lamp used in this study.

TABLE I
EFFECTS OF HIGH INTENSITY RTA LAMPLIGHT ON THE PL INTENSITY AND iV_{OC} OF TOPCON STRUCTURES AT 875 °C

Sample		Before FGA		After FGA	
		PL (a.u.)	iV_{oc} (mV)	PL (a.u.)	iV_{oc} (mV)
As fabricated		41	525	107	537
Without Si wafer cover	N_2	28	491	37	~520
	Air	27	493	45	~520
With Si wafer cover	N_2	501	572	517	588
	Air	519	585	642	618

carried out experiments with samples exposed to RTA intense light along with the samples that were covered with Si wafer cover.

Fig. 9 shows the spectrum of the halogen IR lamp used in the RTA studies. The RTA durations were about 5 min at high temperatures, which was long enough to generate the thermal equilibrium. Approximately, 88.9% of the base 4-in Si wafer received the full spectrum of the RTA lamp radiation, as the test samples only occupied 11.1% of the area. Therefore, the base wafer temperature would be expected to be similar to the one without cover. The Si wafer cover absorbed all of the visible light from the lamp and radiated heat to the test sample. In addition, the temperature readout from the thermocouple touching the base Si wafer indicated the sample temperature.

Fig. 4(a) shows the light-induced degradations of peak PL intensity measured at ~1150 nm without Si wafer cover (denoted by "underlight" legend) for both N_2 and air at different annealing temperatures. The rest of the data were recorded using an Si wafer cover without light exposure. The data from Fig. 4(a) have been summarized and tabulated in Table I. It was observed that under high RTA temperature without the Si wafer cover, there were degradations of iV_{oc}. Later, the post-anneal FGAs recovered from this passivation loss back to the starting passivation quality. It did not improve the iV_{oc} further from the original value. By using the Si wafer cover during RTA and postanneal FGA, it was possible to get higher iV_{oc}. This light-induced degradation occurred irrespective of RTA atmospheres at only high temperatures above 625 °C.

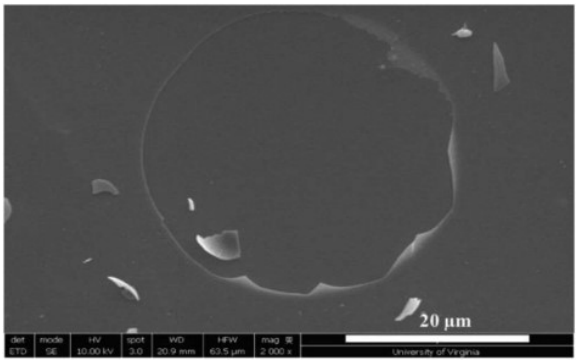

Fig. 10. Top-view SEM image showing a blister formed on the SiN_x:H layer after RTA at 825 °C in N_2.

TABLE II
EFFECTS OF SIN_X:H COATING ON THE PL INTENSITY AND iV_{OC} OF TOPCON STRUCTURES UNDER DIFFERENT RTA ATMOSPHERES AT 825 °C

Sample	Before FGA		After FGA	
	PL (a.u.)	iV_{oc} (mV)	PL (a.u.)	iV_{oc} (mV)
As fabricated	638	622	678	634
RTA in N_2	935	693	1414	706
RTA in Air	730	659	775	672

C. Effect of RTA on SiN_x:H Coated TOPCon Structure

1) Effect on Surface Morphology: An SiN_x:H coated TOPCon sample went through RTA at 825 °C in an N_2 atmosphere. The top-view SEM image in Fig. 10 shows one of the blisters observed on the SiN_x:H layer due to high hydrogen pressure under RTA. The broken SiN_x:H fragments can be observed lying surrounding the blister. The area fraction of blisters was measured as 7%–9% of the total surface area. If the blister formation can be minimized, that would lead to higher iV_{oc} value.

2) Effect on Passivation Quality: Fig. 4(a) shows the peak PL intensity of TOPCon/SiN_x:H test structures annealed by the three-step process at 825 °C under both N_2 and air environments and the subsequent FGAs. All the related data have been summarized and tabulated in Table II. The highest iV_{oc} of 706 mV was achieved after N_2 annealing. For reference, the iV_{oc} of the furnace-annealed p-TOPCon structure reached 688 mV without SiN_x:H and 698 mV with SiN_x:H coating. This displayed the usefulness of using the SiN_x:H layer for passivation purposes. The optical n and k values for as-deposited SiN_x:H film were measured by ellipsometry and were 2.108 and 0.00001, respectively. The SiN_x:H layer would act as an antireflection layer, allowing higher transmission of the excitation laser light and would enhance the PL intensity. However, we are comparing the change in PL intensity between unannealed and annealed samples. The absorption properties of SiN_x:H are assumed to be unchanged after thermal annealing. Therefore, it does not impact

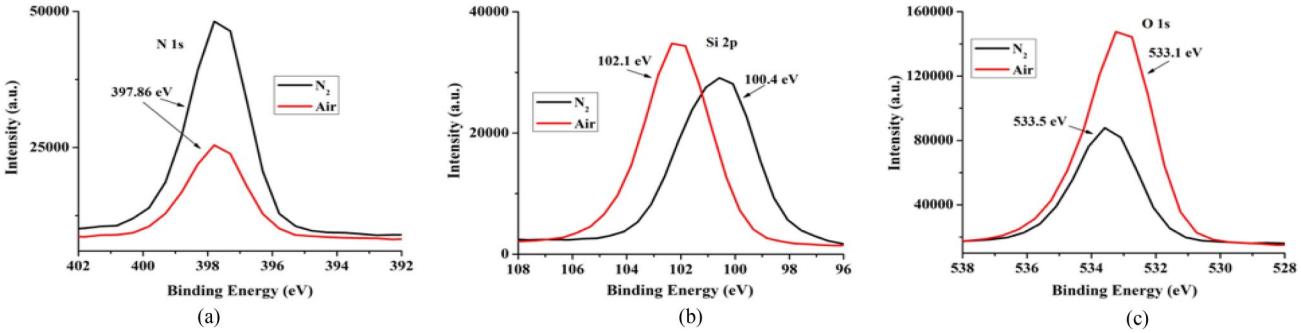

Fig. 11. XPS spectra of (a) N 1s peaks, (b) Si 2p peaks, and (c) O 1s peaks of the TOPCon/SiN_x:H samples after RTA at 825 °C under N_2 and air atmospheres.

the PL measurement, except in the enhancement of absolute PL signal by ∼30% based on the light interference calculations.

3) Effect on SiN_x:H Stoichiometry: Fig. 6(b) and (c) shows the FTIR absorbance spectra of the TOPCon/SiN_x:H structures under N_2 and air annealing at 825 °C and compared with as-deposited film. In Fig. 6(b), it was observed that the wagging mode 1107 cm^{-1} and bending mode 467.8 cm^{-1} peaks of Si-O bond increased after air annealing, which indicated a greater amount of Si-O complexes being formed [45]. The absorbance peak at 612.1 cm^{-1} corresponds to the Si–Si bond. The broad peak centered at 840 cm^{-1} is generally attributed to the presence of the Si-N bond. The spectra from 830.7 to 854.2 cm^{-1} denote the presence of the asymmetric stretching modes of Si-N, which underwent stoichiometric changes likely from Si_3-Si-N to Si_2-(H)Si-N [46]. In Fig. 6(c), it was observed that the presence of the stretching modes of N-H and Si-H peaks at 3325.4 cm^{-1} and 2185.2 cm^{-1}, respectively, in the as-deposited samples showed that they were highly hydrogenated [47]. Later, these peaks disappeared after RTA, which is due to the dehydrogenation.

4) Effect on Chemical Composition of SiN_x:H: Fig. 11 shows the compositional XPS spectra of the TOPCon/SiN_x:H stack annealed at 825 °C both in N_2 and air. In Fig. 11(a), it was observed that there was a comparatively lower count of the N (1s) peak at 397.86 eV in the air-annealed sample than in N_2 annealed. This suggested that there was a decrease in the Si-N bond in the top 3–5 nm thickness of the SiN_x:H layer film after air annealing compared with the N_2 annealing. This is due to the possible Si-O bonds formation on the SiN_x:H surface. In Fig. 11(b), it was observed that there was an Si (2p) peak at 100.4 eV in N_2 annealing and at 102.1 eV in air. The XPS peak at 100.4 eV, observed after N_2 annealing, is attributed to the presence of the Si-Si_3N_1 complex and the peak at 102.1 eV, observed after air annealing, is attributed to the formation of SiO_x complexes [48], [49], [50], [51]. The Si-N peak is expected to be located at 101.7 eV, and the SiO_2 peak to be at 103.5 eV, but peak positions are sensitive to stoichiometry [52]. Finally, after air annealing, the intensity of O (1s) peak at 533.1 eV was higher as compared with N_2 annealing, as shown in Fig. 11(c). This proved that there were more surficial SiO_2 and stoichiometric changes that occurred during the air annealing, as previously showed by Miller and Linton [53] and Lin and Hwu [54].

The results on crystallinity property determination by Raman spectroscopy, chemical changes by FTIR and XPS, and electrical property changes by sheet resistance measurement have been presented. As the annealing temperature increases, the poly-Si crystalline fraction and iV_{oc} increase, implying lower charge-carrier recombination. The FTIR measurements were not sensitive to detect the passivation quality; however, it detects dehydrogenation in SiN_x:H capped samples. The depth-profiling XPS measurements show higher concentration of oxygen in the ultrathin oxide after air annealing, which could lead to higher iV_{oc} compared with that of N_2 for uncapped samples. The surface morphology shows the blister formation affecting the carrier selectivity and, hence, the surface passivation.

IV. Conclusion

In this article, the effect of RTA atmosphere on surface morphology (blister formation), surface passivation, changes in polysilicon crystallinity, composition, sheet resistance, and determination of oxidation state of ultrathin SiO_2 passivation layer in *in situ* B-doped poly-Si-based p-TOPCon was investigated. Second, it was discovered that the high-intensity light exposure during RTA significantly degraded the surface passivation quality and, hence, iV_{oc}. Third, first depositing an SiN_x:H layer on top of polysilicon and carrying out a single step of RTA provide a high iV_{oc} value of 706 mV. In summary, this article shows the following.

1) During annealing, hydrogen-induced blisters must be minimized as confirmed by the PL measurements in which they lead to the loss of surface passivation.
2) A higher iV_{oc} was observed under air RTA compared with nitrogen in SiN_x:H-uncapped samples,
3) UV and visible light radiation during high-temperature RTA induces degradation and its exposure must be avoided during the annealing process.
4) The Si-O bond changes from wagging mode to stretching mode under annealing at 875 °C.
5) The RTA can provide low sheet resistance value of 0.9 kΩ/sq for a 30 nm *in situ* B-doped polysilicon film.
6) Under RTA, the fraction of polycrystalline phase maximizes at around 825 °C.
7) RTA in N_2 of SiN_x:H coated polysilicon film provided the higher iV_{oc} compared with uncoated film.
8) RTA can provide iV_{oc} value similar to the furnace annealing.

The initial hydrogen content in the as-deposited TOPCon structure should be minimized to avoid blister formation, and the LPCVD of *in situ* B-doped a-Si:H should be done at 588 °C to minimize hydrogen incorporation as well as to obtain a higher poly-crystalline fraction.

ACKNOWLEDGMENT

The authors would like to thank the NSF MRI Award #1626201 for using PHI Versaprobe III XPS (UVA NMCF) instrument to obtain the XPS data.

REFERENCES

[1] L. Galleni et al., "Mechanisms of charge carrier transport in polycrystalline silicon passivating contacts," *Sol. Energy Mater. Sol. Cells*, vol. 232, 2021, Art. no. 111359, doi: 10.1016/j.solmat.2021.111359.

[2] M. Fırat et al., "Local enhancement of dopant diffusion from polycrystalline silicon passivating contacts," *ACS Appl. Mater. Interfaces*, vol. 14, no. 15, pp. 17975–17986, Apr. 2022, doi: 10.1021/acsami.2c01801.

[3] F. Haase et al., "Laser contact openings for local poly-Si-metal contacts enabling 26.1%-efficient POLO-IBC solar cells," *Sol. Energy Mater. Sol. Cells*, vol. 186, pp. 184–193, 2018, doi: 10.1016/j.solmat.2018.06.020.

[4] A. Richter et al., "n-type Si solar cells with passivating electron contact: Identifying sources for efficiency limitations by wafer thickness and resistivity variation," *Sol. Energy Mater. Sol. Cells*, vol. 173, pp. 96–105, 2017, doi: 10.1016/j.solmat.2017.05.042.

[5] Y. Tao, V. Upadhyaya, K. Jones, and A. Rohatgi, "Tunnel oxide passivated rear contact for large area n-type front junction silicon solar cells providing excellent carrier selectivity," *AIMS Mater. Sci.*, vol. 3, no. 1, pp. 180–189, Jan. 2016, doi: 10.3934/matersci.2016.1.180.

[6] S. Choi et al., "Formation and suppression of hydrogen blisters in tunnelling oxide passivating contact for crystalline silicon solar cells," *Sci. Rep.*, vol. 10, no. 1, Jun. 2020, Art. no. 9672, doi: 10.1038/s41598-020-66801-4.

[7] T. Gao et al., "An industrially viable TOPCon structure with both ultrathin SiO_x and n+poly-Si processed by PECVD for p-type c-Si solar cells," *Sol. Energy Mater. Sol. Cells*, vol. 200, 2019, Art. no. 109926, doi: 10.1016/j.solmat.2019.109926.

[8] F. Feldmann, M. Bivour, C. Reichel, M. Hermle, and S. W. Glunz, "Passivated rear contacts for high-efficiency n-type Si solar cells providing high interface passivation quality and excellent transport characteristics," *Sol. Energy Mater. Sol. Cells*, vol. 120, 2014, pp. 270–274, doi: 10.1016/j.solmat.2013.09.017.

[9] A. Harter et al., "Influence of intrinsic silicon layer and intermediate silicon oxide layer on the performance of inline PECVD deposited boron-doped TOPCon," *IEEE J. Photovolt.*, vol. 11, no. 4, pp. 936–943, Jul. 2021, doi: 10.1109/JPHOTOV.2021.3071220.

[10] F. Feldmann et al., "Efficient carrier-selective p- and n-contacts for Si solar cells," *Sol. Energy Mater. Sol. Cells*, vol. 131, pp. 100–104, 2014, doi: 10.1016/j.solmat.2014.05.039.

[11] U. Römer et al., "Recombination behavior and contact resistance of n+ and p+ poly-crystalline Si/mono-crystalline Si junctions," *Sol. Energy Mater. Sol. Cells*, vol. 131, pp. 85–91, 2014, doi: 10.1016/j.solmat.2014.06.003.

[12] P. Borden et al., "Polysilicon tunnel junctions as alternates to diffused junctions," in *Proc. 23rd Eur. Photovolt. Sol. Energy Conf. Exhib.*, Valencia, Spain, 2008, pp. 1149–1152, doi: 10.4229/23rdEUPVSEC2008-2DO.1.4.

[13] A. Ingenito et al., "A passivating contact for silicon solar cells formed during a single firing thermal annealing," *Nature Energy*, vol. 3, no. 9, pp. 800–808, 2018, doi: 10.1038/s41560-018-0239-4.

[14] M. Feng et al., "Rapid-thermal-annealing-induced passivation degradation and recovery of polysilicon passivated contact with Czochralski and cast multicrystalline silicon substrates," *Physica Status Solidi A, Appl. Mater. Sci.*, vol. 218, no. 21, 2021, Art. no. 2100344, doi: 10.1002/pssa.202100344.

[15] Q. Yang et al., "In-situ phosphorus-doped polysilicon prepared using rapid-thermal anneal (RTA) and its application for polysilicon passivated-contact solar cells," *Sol. Energy Mater. Sol. Cells*, vol. 210, 2020, Art. no. 110518, doi: 10.1016/j.solmat.2020.110518.

[16] C. Reichel et al., "Tunnel oxide passivated contacts formed by ion implantation for applications in silicon solar cells," *J. Appl. Phys.*, vol. 118, no. 20, 2015, Art. no. 205701, doi: 10.1063/1.4936223.

[17] C. Lee et al., "Amorphous silicon thin film deposition for poly-Si/SiO_2 contact cells to minimize parasitic absorption in the near-infrared region," *Energies*, vol. 14, no. 24, Dec. 2021, Art. no. 8199, doi: 10.3390/en14248199.

[18] B. W. H. van de Loo et al., "On the hydrogenation of poly-Si passivating contacts by Al_2O_3 and SiN_x thin films," *Sol. Energy Mater. Sol. Cells*, vol. 215, 2020, Art. no. 110592, doi: 10.1016/j.solmat.2020.110592.

[19] B. Steinhauser et al., "On the influence of the SiNx composition on the firing stability of poly-Si/SiN_x stacks," *Physica Status Solidi A, Appl. Mater. Sci.*, vol. 217, no. 21, 2020, Art. no. 2000333, doi: 10.1002/pssa.202000333.

[20] C. Hollemann et al., "Firing stability of tube furnace-annealed n-type poly-Si on oxide junctions," *Prog. Photovolt.: Res. Appl.*, vol. 30, no. 1, pp. 49–64, 2022, doi: 10.1002/pip.3459.

[21] G. Nogay et al., "Interplay of annealing temperature and doping in hole selective rear contacts based on silicon-rich silicon-carbide thin films," *Sol. Energy Mater. Sol. Cells*, vol. 173, pp. 18–24, Dec. 2017, doi: 10.1016/j.solmat.2017.06.039.

[22] D. Kang et al., "Comparison of firing stability between p- and n-type polysilicon passivating contacts," *Prog. Photovolt., Res. Appl.*, vol. 30, no. 8, pp. 970–980, 2022, doi: 10.1002/pip.3544.

[23] V. Arya et al., "Laser ablation and Ni/Cu plating approach for tunnel oxide passivated contacts solar cells with variate polysilicon layer thickness: Gains and possibilities in comparison to screen printing," *Physica Status Solidi A, Appl. Mater. Sci.*, vol. 217, no. 24, 2020, Art. no. 2000474, doi: 10.1002/pssa.202000474.

[24] R. C. G. Naber, B. W. H. van de Loo, and J. R. M. Luchies, "LPCVD in-situ n-type doped polysilicon process throughput optimization and implementation into an industrial solar cell process flow," in *Proc. 36th Eur. Photovolt. Sol. Energy Conf. Exhib.*, 2019, pp. 180–183.

[25] C.-A. Chang, "On the enhancement of silicon chemical vapor deposition rates at low temperatures," *J. Electrochem. Soc.*, vol. 123, no. 8, pp. 1245–1247, 1976, doi: 10.1149/1.2133045.

[26] W.-J. Choi et al., "Optimization of in-situ and ex-situ doped p+ passivating contact for high efficiency p-TOPCon solar cell application," in *Proc. IEEE 48th Photovolt. Specialists Conf.*, 2021, pp. 1907–1912, doi: 10.1109/PVSC43889.2021.9518759.

[27] A. de Calheiros Velozo, G. Lavareda, C. Nunes de Carvalho, and A. Amaral, "Thermal dehydrogenation of amorphous silicon deposited on c-Si: Effect of the substrate temperature during deposition," *Physica Status Solidi C, Curr. Topics Solid State Phys.*, vol. 9, no. 10/11, pp. 2198–2202, 2012, doi: 10.1002/pssc.201200194.

[28] A. Sinha, A. Soman, U. Das, S. Hegedus, and M. C. Gupta, "Nanosecond pulsed laser patterning of interdigitated back contact heterojunction silicon solar cells," *IEEE J. Photovolt.*, vol. 10, no. 6, pp. 1648–1656, Nov. 2020, doi: 10.1109/JPHOTOV.2020.3026907.

[29] A. V. Naumkin, A. Kraust-Vass, S. W. Gaarenstroom, and C. J. Powell, "NIST X-ray photoelectron spectroscopy database, national institute of standards and technology," Nat. Inst. Standards Technol, Gaithersburg, MD, USA, 2000.

[30] D. K. Agarwal, N. Maheshwari, S. Mukherji, and V. R. Rao, "Asymmetric immobilization of antibodies on a piezo-resistive micro-cantilever surface," *RSC Adv.*, vol. 6, no. 21, pp. 17606–17616, Feb. 2016, doi: 10.1039/c6ra01440b.

[31] H. Schröder, E. Obermeier, and A. Steckenborn, "Micropyramidal hillocks on KOH etched {100} silicon surfaces: Formation, prevention and removal," *J. Micromech. Microeng.*, vol. 9, no. 2, pp. 139–145, 1999, doi: 10.1088/0960-1317/9/2/309.

[32] Q. Li et al., "Replacing the amorphous silicon thin layer with microcrystalline silicon thin layer in TOPCon solar cells," *Sol. Energy*, vol. 135, pp. 487–492, 2016, doi: 10.1016/j.solener.2016.06.012.

[33] U. Rau, "Reciprocity relation between photovoltaic quantum efficiency and electroluminescent emission of solar cells," *Phys. Rev. B*, vol. 76, no. 8, 2007, Art. no. 085303, doi: 10.1103/PhysRevB.76.085303.

[34] C. B. Saltonstall, J. Serrano, P. M. Norris, P. E. Hopkins, and T. E. Beechem, "Single element Raman thermometry," *Rev. Sci. Instrum.*, vol. 84, no. 6, 2013, Art. 064903, doi: 10.1063/1.4810850.

[35] T. N. Tran, T. V. A. Pham, M. L. P. Le, T. P. T. Nguyen, and V. M. Tran, "Synthesis of amorphous silica and sulfonic acid functionalized silica used as reinforced phase for polymer electrolyte membrane," *Adv. Natural Sci.: Nanosci. Nanotechnol.*, vol. 4, no. 4, 2013, Art. no. 045007, doi: 10.1088/2043-6262/4/4/045007.

[36] M. Watanabe and N. Takenawa, "FTIR measurement of nitrogen in silicon using shuttle type sample stage," *Proc. - Electrochem. Soc.*, vol. 5, pp. 121–131, 2004.

[37] L. X. Yi, J. Heitmann, R. Scholz, and M. Zacharias, "Phase separation of thin SiO layers in amorphous SiO/SiO_2 superlattices during annealing," *J. Phys., Condens. Matter*, vol. 15, no. 39, pp. S2887–S2895, Sep. 2003, doi: 10.1088/0953-8984/15/39/012.

[38] T. Jutarosaga, J. S. Jeoung, and S. Seraphin, "Infrared spectroscopy of Si–O bonding in low-dose low-energy separation by implanted oxygen materials," *Thin Solid Films*, vol. 476, no. 2, pp. 303–311, Apr. 2005, doi: 10.1016/j.tsf.2004.10.006.

[39] S. Matsuda et al., "Correlation between temperature coefficient of elasticity and Fourier transform infrared spectra of silicon dioxide films for surface acoustic wave devices," *IEEE Trans. Ultrasonics, Ferroelectr., Freq. Control*, vol. 58, no. 8, pp. 1684–1687, Aug. 2011, doi: 10.1109/TUFFC.2011.1996.

[40] T. F. Young, C. P. Chen, J. F. Liou, Y. L. Yang, and T. C. Chang, "Study on the Si–Si vibrational states of the near surface region of porous silicon," *J. Porous Mater.*, vol. 7, no. 1, pp. 339–343, 2000, doi: 10.1023/a:1009622601723.

[41] G. Betz and G. K. Wehner, "Sputtering of multicomponent materials," in *Sputtering by Particle Bombardment II: Sputtering of Alloys and Compounds, Electron and Neutron Sputtering, Surface Topography*, 1st ed., vol. 52, R. Behrish, Ed. Berlin, Germany: Springer, 1983, pp. 11–90.

[42] R. Alfonsetti, L. Lozzi, M. Passacantando, P. Picozzi, and S. Santucci, "XPS studies on SiOx thin films," *Appl. Surf. Sci.*, vol. 70–71, pp. 222–225, 1993, doi: 10.1016/0169-4332(93)90431-A.

[43] I. Lisovskyy et al., "Transformation of the structure of silicon oxide during the formation of Si nanoinclusions under thermal annealing," *Ukrainian J. Phys.*, vol. 54, no. 4, pp. 383–390, 2009.

[44] C.-M. Park et al., "Characterizations and electrochemical behaviors of disproportionated SiO and its composite for rechargeable Li-ion batteries," *J. Mater. Chem.*, vol. 20, no. 23, pp. 4854–4860, 2010, doi: 10.1039/b923926j.

[45] B. B. Zviagina, V. A. Drits, and O. V. Dorzhieva, "Distinguishing features and identification criteria for K-dioctahedral 1*M* micas (Illite-aluminoceladonite and illite-glauconite-celadonite series) from middle-infrared spectroscopy data," *Minerals*, vol. 10, no. 2, 2020, Art. no. 153, doi: 10.3390/min10020153.

[46] G. Scardera, T. Puzzer, G. Conibeer, and M. A. Green, "Fourier transform infrared spectroscopy of annealed silicon-rich silicon nitride thin films," *J. Appl. Phys.*, vol. 104, no. 10, 2008, Art. no. 104310, doi: 10.1063/1.3021158.

[47] I. Guler, "Optical and structural characterization of silicon nitride thin films deposited by PECVD," *Mater. Sci. Eng., B*, vol. 246, pp. 21–26, 2019, doi: 10.1016/j.mseb.2019.05.024.

[48] A. Kitao, K. Imakita, I. Kawamura, and M. Fujii, "An investigation into second harmonic generation by Si-rich SiN_x thin films deposited by RF sputtering over a wide range of Si concentrations," *J. Phys. D, Appl. Phys.*, vol. 47, no. 21, 2014, Art. no. 215101, doi: 10.1088/0022-3727/47/21/215101.

[49] W. A. M. Aarnink, A. Weishaupt, and A. van Silfhout, "Angle-resolved X-ray photoelectron spectroscopy (ARXPS) and a modified Levenberg-Marquardt fit procedure: A new combination for modeling thin layers," *Appl. Surf. Sci.*, vol. 45, no. 1, pp. 37–48, Aug. 1990, doi: 10.1016/0169-4332(90)90018-U.

[50] J. Finster, E. D. Klinkenberg, J. Heeg, and W. Braun, "ESCA and SEXAFS investigations of insulating materials for ULSI microelectronics," *Vacuum*, vol. 41, no. 7/9, pp. 1586–1589, 1990, doi: 10.1016/0042-207X(90)94025-L.

[51] X. Zhao, M. Leavy, N. P. Magtoto, and J. A. Kelber, "Copper wetting of a tantalum silicate surface: Implications for interconnect technology," *Appl. Phys. Lett.*, vol. 79, no. 21, pp. 3479–3481, 2001, doi: 10.1063/1.1418025.

[52] M. Biesinger, "X-ray photoelectron spectroscopy (XPS) reference pages," Accessed on: Apr. 24, 2022. [Online]. Available: http://www.xpsfitting.com/2012/01/silicon.html

[53] M. L. Miller and R. W. Linton, "X-ray photoelectron spectroscopy of thermally treated silica SiO_2 surfaces," *Anal. Chem.*, vol. 57, no. 12, pp. 2314–2319, 1985, doi: 10.1021/ac00289a033.

[54] Y.-P. Lin and J.-G. Hwu, "Quality improvement in LPCVD silicon nitrides by anodic and rapid thermal oxidations," *Electrochem. Solid-State Lett.*, vol. 7, no. 5, 2004, Art. no. G87, doi: 10.1149/1.1664053.